

COSMOLOGY LARGE ANGULAR SCALE SURVEYOR: 40 GHZ TELESCOPE BEAM AND POINTING CALIBRATION

ZHILEI XU (徐智磊)^{1,2}, PEDRO FLUXÁ ROJAS,³ BASTIÁN PRADENAS,⁴ AND AUTHOR D⁵

¹*Department of Physics and Astronomy, Johns Hopkins University 3701 San Martin Drive, Baltimore, MD, USA*

²*Department of Physics and Astronomy, University of Pennsylvania 209 S 33rd St, Philadelphia, PA, USA*

³*Instituto de Astrofísica, Pontificia Universidad Católica de Chile*

⁴*Grupo de Cosmología y Astrofísica Teórica, Departamento de Física, FCFM, Universidad de Chile, Blanco Encalada 2008, Santiago, Chile.*

⁵*Affiliation 4*

ABSTRACT

The Cosmology Large Angular Scale Surveyor (CLASS) is an array of telescopes that observes the cosmic microwave background (CMB) polarization over 70% of the sky from the Atacama Desert, Chile in frequency bands at 40 GHz, 90 GHz, 150 GHz, and 220 GHz. CLASS is making large angular scale CMB polarization measurements as part of a five-year survey that will constrain the primordial fluctuation tensor-to-scalar ratio at the 0.01 level and measure the optical depth to last scattering to near the cosmic variance limit. This paper presents the pointing and beam calibration of the 40 GHz telescope during the observation from July 2016 to March 2018. The pointing and beam calibration are performed by observing the Moon. The pointing are stable within 1 arcminute ($< 1\%$ of the beam full width half maximum); while the beam follows the profile expected from the optical model from GRASP simulation. The window function is calculated from the measured beam profile.

Keywords: CMB polarization, CLASS, pointing and beam calibration

1. INTRODUCTION

The discovery of the cosmic microwave background (CMB) (Penzias and Wilson 1965) started the era of modern cosmology. The CMB spectrum was measured to follow a blackbody spectrum at 2.728 ± 0.004 K (95% CL), with root-mean-square deviation of less than 50 parts per million of the spectrum peak (Fixsen et al. 1996). The CMB temperature anisotropy across the sky, at the level of around 10 parts per million, was then discovered (Bennett et al. 1996; Hinshaw et al. 2013; Planck Collaboration et al. 2016). The CMB spectrum and temperature anisotropy measurements are successfully explained by the Λ CDM cosmology model, whereas it does not provide physical reasons for the fine-tuned origin of the universe. Different theories were proposed to answer these questions. To verify the correct theory, the most powerful probe is the CMB polarization anisotropy at large angular scales (Kamionkowski et al. 1997; Seljak and Zaldarriaga 1997). The CMB polarization anisotropy is even lower the 10-parts-per-million temperature anisotropy. Measuring this pattern, especially across large fraction of the sky, is a challenging technical task. The Cosmology large angular scale surveyor (CLASS) is built to accomplish this task.

The Cosmology Large Angular Scale Surveyor (CLASS) is an array of telescopes that observes Cosmic Microwave Background (CMB) polarization over 70% of the sky from

the Atacama Desert, Chile in frequency bands at 40 GHz, 90 GHz, 150 GHz, and 220 GHz. Multi-frequency observation enables CLASS to distinguish the CMB from galactic foregrounds. CLASS is making large angular scale CMB polarization measurements as part of a five-year survey that will constrain the primordial fluctuation tensor-to-scalar ratio at the 0.01 level by measuring both the reionization and recombination peaks. CLASS will measure the optical depth to last scattering to near the cosmic variance limit, significantly improving on current constraints (Watts et al. 2018). Combining the CLASS optical depth measurement with higher resolution CMB data (BAO refs?(BOSS?)) will improve constraints on the sum of neutrino masses (Allison et al. 2015). CLASS will also provide the deepest wide-sky-area Galactic microwave polarization maps for Galactic studies.

The first observing campaign starts with the 40 GHz telescope from June 2016 to March 2018. This paper will discuss the pointing and beam calibration, physical optics simulation, and window function from the measurements. Section 3 introduces the calibration sources and their radio properties. The calibration method is discussed in Section ?? . Pointing results are presented in Section 5. Section 6 presents intensity beam calibration results. Polarization beam results are discussed in Section 9. Optical modeling and simulation is presented in Section 10. Window functions for cosmological studies are discussed in Section 8. The far sidelobe studies are presented in Section 11.

Bastian also talked about moon simulation in the window function section. We will have it resolved to avoid redundancy.

2. INSTRUMENT

The 40 GHz CLASS telescope design is shown in Figure 1. [ZX: I probably need to change the focal plane beam map into an array pointing plot with crosses.] The telescope design contains the variable-delay polarization modulator (VPM), the primary and secondary mirror and the cryogenic receiver. [ZX: probably should denote the components in the plot.]

The CLASS 40 GHz cryogenic receiver contains 36 feedhorns, pairwise coupled to 72 sensors for orthogonal polarization directions. During the first observing campaign, 64 of the sensors were optical sensitive while all of the feedhorns are coupled to at least one sensor. The average saturation power and noise equivalent power (NEP) of the detectors are measured to be 6.3 pW and 19 aW \sqrt{s} (Appel et al. 2014) [ZX: to be updated.]. Optically, the full width at half maximum (FWHM) of each beam is designed to be $\sim 1.5^\circ$ (Eimer et al. 2012). [ZX: Could probably been updated with Pedro's simulation]. Given the specification of the telescope, the Moon and Taurus A were selected as the calibration sources.

The CLASS Q-band telescope sits on a three-axis mount that provides azimuth, elevation, and boresight rotations. The mount rotates 720° in azimuth and from 20° to 90° in elevation. The azimuth and elevation rotation enables the telescope to point anywhere on the sky. However, the polarization signal is more than just one amplitude. The additional boresight rotation keeps the pointing unchanged while rotates the detector polarization direction on the sky from -45° to $+45^\circ$, sampling the polarization signal in a wider parameter space.

3. CALIBRATION SOURCES

The CLASS 40 GHz telescope contains 36 feedhorns, pairwise coupled to 72 sensors for orthogonal polarization directions. During the first observing campaign, 64 of the sensors were optical sensitive while all of the feedhorns are coupled to at least one sensor. The average saturation power and noise equivalent power (NEP) of the detectors are measured to be 6.3 pW and 19 aW \sqrt{s} (Appel et al. 2014) [ZX: to be updated.]. Optically, the full width at half maximum (FWHM) of each beam is designed to be $\sim 1.5^\circ$ (Eimer et al. 2012). Given the specification of the telescope, the Moon and Taurus A were selected as the calibration sources.

3.1. Moon Properties

The angular diameter of the Moon is $\sim 0.5^\circ$, one third of the CLASS 40 GHz beam full width half maximum (FWHM). The 1.5° beam is enlarged by $\sim 0.05^\circ$ after being convolved by the Moon, demonstrating the angular size of the Moon is small enough for CLASS 40 GHz telescope pointing and beam calibration.

The thermal properties of the Moon have been studied by the Chang'E lunar satellite mission (Zheng et al. 2012). Tem-

perature data are measured at different lunar latitudes across 360° lunar hour angles at 37 GHz. The phase of the Moon is simulated with different part of the hour angles facing the Earth. Assuming the Moon regolith as a blackbody, the upper limit of the observed intensity can be estimated between $1 \sim 2$ pW observed by the telescope, within the saturation power ~ 6.8 pW. The noise level is estimated, assuming 1 s integration time, as ~ 11 aW. The Moon, as a calibration source, is bright enough for us to study the beam with $\sim 10^5$ signal-to-noise ratio, while it is not too bright to saturate the detectors.

Beside temperature, the Moon is also a polarization calibration source. According to the Fresnel equations, the polarization of the Moon can be parametrized as:

$$R_s = \frac{\left| \sqrt{\varepsilon} \cos \theta_i - \cos \theta_t \right|^2}{\left| \sqrt{\varepsilon} \cos \theta_i + \cos \theta_t \right|^2}, \quad (1)$$

$$R_p = \frac{\left| \sqrt{\varepsilon} \cos \theta_t - \cos \theta_i \right|^2}{\left| \sqrt{\varepsilon} \cos \theta_t + \cos \theta_i \right|^2}, \quad (2)$$

where R_s , R_p are the polarization components with the electric field perpendicular and parallel to the plane of incidence, θ_i and θ_t are the angles that incident and transmitted rays make to the normal of the interface surface, and ε is the dielectric constant of the Moon regolith. The difference between refracted s-wave and p-wave results in net polarization in lunar radiation. The polarization fraction depends on the refraction angle θ_t . Due to symmetry, there is no net polarization at the center of the Moon, while the polarization fraction increases from the center to the limb (Zhang et al. 2012). The polarization intensity is calculated with the brightness temperature and the polarization fraction. The linear polarization pattern, which is a vector field, can be conveniently expressed by maps of Stokes parameters, say Stokes U ($\pm 45^\circ$ polarization directions). Accounting for the CLASS 1.5° beam, the measured Moon intensity and Stokes U maps are shown in Figure 2.

3.2. Taurus A

This needs to be investigated. I don't have any simulation results at hand but will look into this.

4. MOON DATA AND INTENSITY ANALYSIS

To calibrate the pointing and the beam of the telescope, dedicated Moon scans are performed. The data are analyzed with specialized software to produce pointing and beam calibration results.

During CMB observations, the CLASS 40 GHz telescope stays at 45° elevation and scans across 720° azimuth. As the Earth spins, the telescopes covers $> 70\%$ of the sky two rounds [ZX: how to express this better?] everyday. In order to emulate the CMB observations, the calibration observation is conducted at the same 45° elevation. When the Moon rises high enough to be observed by all detectors in the focal plane array, two Moon scans are performed during the Moon rising and setting. During each Moon scan, the telescope scans

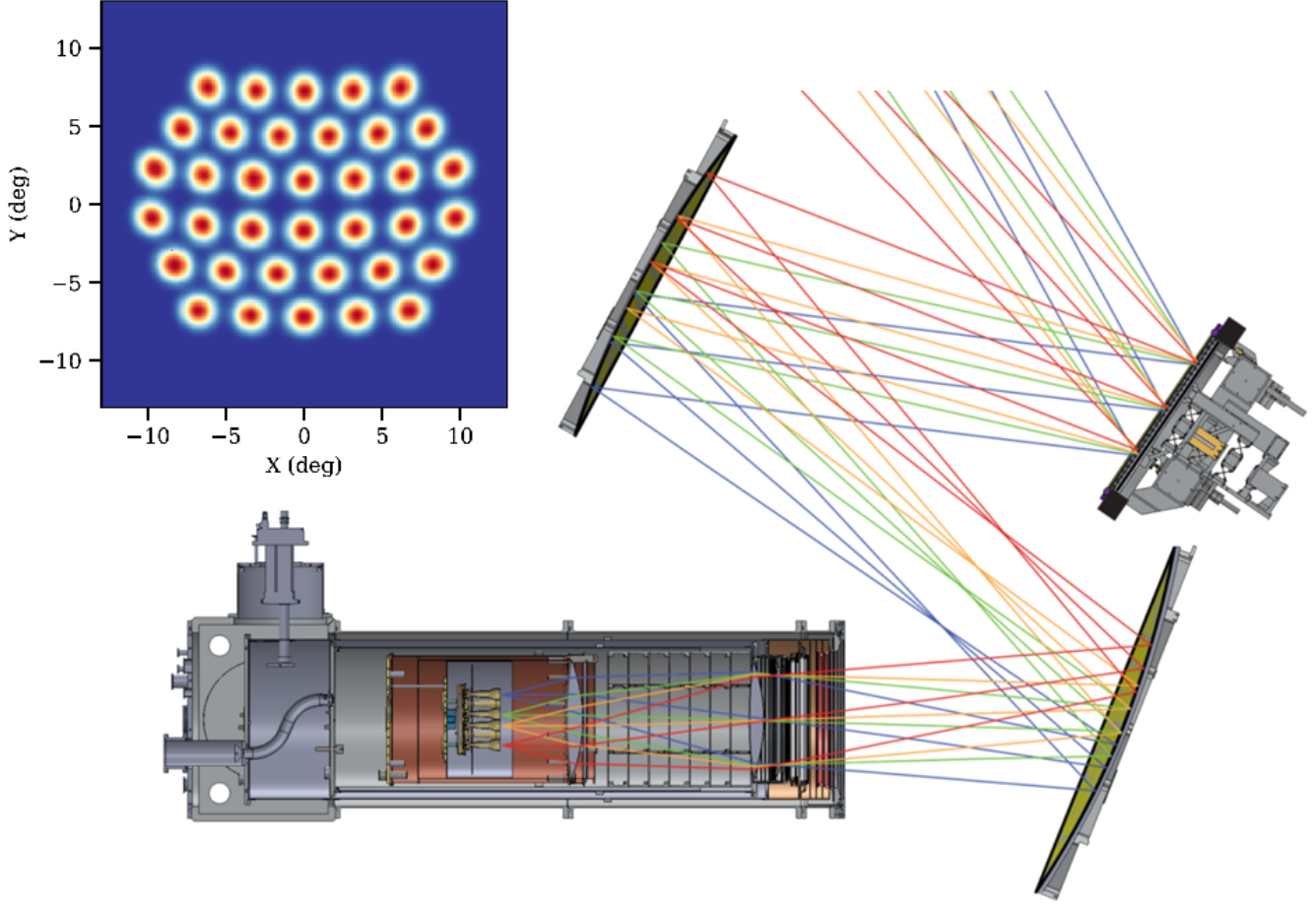


Figure 1. The CLASS 40 GHz band telescope design and measured focal plane beam map.

$\pm 13^\circ$ in azimuth. Considering the 20° field of view, this azimuthal scan range enables each detector to sample around the Moon with $> 3^\circ$ margin.

During each Moon scan, each detector collects a series of time-ordered data (TOD). The data first went through several basic processing as described in a companion paper (cite Lucas's paper?), before they enter the pointing analysis.

The telescope boresight pointing (including boresight rotation) has the nominal values calculated from the telescope encoder readings. A new spherical coordinate system is defined with the boresight pointing at the origin and x/y axis perpendicular/parallel to the telescope optical plane. This coordinate system is called the “telescope coordinate system”, which is locked to the boresight pointing and rotation. The Moon position on the sky coordinates is also converted into the telescope coordinate system via Quaternion rotations. In the telescope coordinate system, only the Moon moves during Moon scans, as shown in Figure 3.

In the telescope coordinate system, each detector points at set angular offsets X_{offset} , Y_{offset} . With the detector data and the corresponding Moon positions in the telescope coordinate system, a map is generated for each detector. In these maps, the Moon intensity signal (as shown in Figure 2) appears at different positions, which gives the angular offsets of all the

detectors. Pointings from all the detectors form an array pattern. The array pattern should be level and centered at the origin of the telescope coordinate system. Any deviation indicates the offset between the encoder readings and the true boresight pointing (The leveling is related to the boresight rotation while the centering is related to the boresight pointing in azimuth and elevation). The boresight pointing offset information feeds back into the telescope pointing model to correct the boresight pointing deviations. With the corrected boresight pointing, pointing offsets for each detector are fit again. Through this iterative procedure, the boresight pointing and detector pointing offsets together provide detector pointing on the sky.

Beyond pointing, Moon scans also calibrate the angular response of each detector on the sky (i.e., the beam). In the telescope coordinate system, the Moon appears to zigzag across the array during Moon scans (Figure 3). With the knowledge of a certain detector pointing offset, another coordinate system is defined with the detector at the origin, with the y-axis pointing along the local meridian in the telescope coordinate system, and the x-axis points to the right perpendicular to the y-axis. This “detector coordinate system” is the natural coordinate system for a beam map. The high intensity signal from the Moon provides high signal-to-noise beam maps for each

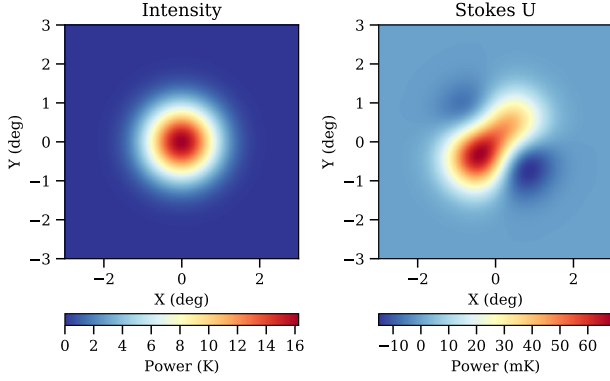


Figure 2. Model of the Moon maps measured by the CLASS 40 GHz telescope. *Left:* The Moon intensity map is generated from the data in Zheng et al. (2012) at the phase of full Moon. The map is obtained by convolving the Moon intensity map with a 1.5° FWHM Gaussian beam. *Right:* The Moon polarization (Stokes U) is calculated with the Fresnel equations from the intensity map, and convolved by a 1.5° FWHM Gaussian beam. The uneven power of the quadrupole pattern results from the nonuniform temperature on the Moon surface, even at full Moon. The amplitude of the Stokes U map is three orders of magnitude lower than the intensity one.

Table 1. Moon Scan Counts at Different Boresight Angles

Boresight Angle	Moon Scan Count	Percentage
-45°	19	18.3%
-30°	11	10.6%
-15°	10	9.6%
0°	22	21.1%
$+15^\circ$	10	9.6%
$+30^\circ$	10	9.6%
$+45^\circ$	22	21.1%

detector. Following the same method, high signal-to-noise beam maps are provided for each detector in the array.

5. POINTING

Results in this section need to be updated with data from the entire season.

Around 300 [ZX: get exact number covering dedicated/pseudo moon scans, should also mention the distribution of boresight angle here.] Moon scans were performed at different boresight angles from July 2016 to October 2017, details can be found in Table 1.

Maybe we should show the boresight pointing first and then the pointing offsets.

The detector offsets from boresight are shown in Figure 4. These positions are consistent with the optical design (Eimer

et al. 2012). Standard deviations (σ_X , σ_Y), computed across the ~ 300 Moon scans, are inflated by a factor of 60 as plotted in Figure 4, meaning that a standard deviation of 1° in Figure 4 corresponds to 1 arcmin. Given the 1.5° beam size, the standard deviations (typically < 1 arcmin) is around 1% of the beam size. The arcminute-scale differential pointing between paired detectors (Δ_X and Δ_Y) are also included in Figure 4 ([ZX: Not inflated but probably should]). Histograms on the four pointing parameters (pointing standard deviations σ_X , σ_Y and paired detector differential pointing Δ_X , Δ_Y) are presented in Figure 5 [ZX: (This plot should be remade with the entire Era1 data to see whether it is worth to stay)].

The warm-optics supporting structure reaches its maximum deformation at $\pm 45^\circ$ boresight angles toward opposite directions. The deformations affect the positions of the optical components and eventually leads to pointing deviations. The supporting structure was designed to constrain the maximum deformation within 1 mm. From $+45^\circ$ to -45° boresight angle, pointing deviations along the X direction should follow a continuous rising trend over ~ 1.2 arcmin; pointing deviations along Y direction should follow a flat trend. Beyond the boresight angle dependence, pointing dependence on time is designed to be stable within the five-year survey time.

With Moon scans across the whole season performed at different boresight angles, the pointing dependence on boresight angle and time is characterized. Figure 6 shows the results for one typical detector. The trend and the amplitude of the boresight rotation dependence are consistent with the estimation from the warm-optics support structure design. The stability of the pointing across multiple months is within 1 arcmin ($\sim 1\%$ of the beam FWHM). Although the result is from one typical detector, the conclusion holds across all the detectors.

Should I also show the array plots on the time/boresight rotation dependence?

6. BEAM MAPS

As introduced in Section 4, beam maps for each detector are provided from each Moon scan. Given ~ 300 Moon scans, each detector has ~ 300 individual beam maps. A selection function rejects sub-optimal beam maps according to several criteria, including weather condition, detector noise level, and detector stability etc. Typically, > 250 beam maps are accepted for each detector. The accepted beam maps are normalized by the fitted peak amplitude before they are stacked to form a stacked beam map for one detector. Boresight rotation rotates the detector array pattern on the sky, enabling each detector to sample the Moon at different angles. Therefore, stacked beam maps extend to 10° for all the detectors.

Figure 7 shows the stacked beam map for one typical detector. This beam map contains around eight million data points (800,000 seconds) from 300 different Moon scans. The beam map color scale is set to be logarithmic from 10^{-1} to 10^{-4} (normalized at the peak); this color scale is selected

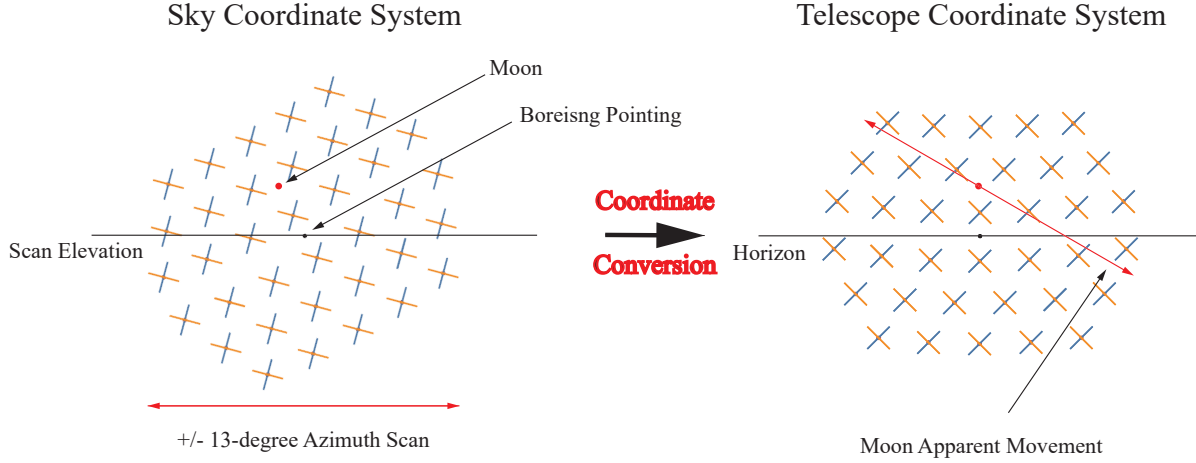


Figure 3. Moon scan illustration and coordinate systems. *Left:* The detector array is presented, centered at the scan elevation with a boresight rotation. The Moon slowly rises or sets as the telescope scans $\pm 13^\circ$ in azimuth. Both the Moon positions and the boresight pointings are described in “sky coordinate system”. *Right:* The Moon positions are converted into the “telescope coordinate system”, where the boresight pointing is the origin and x/y axis pointing perpendicular/parallel to the telescope optical plane. In the telescope coordinate system, every detector is fixed at set Δx and Δy angular offsets while the Moon appears to zigzag across the array.

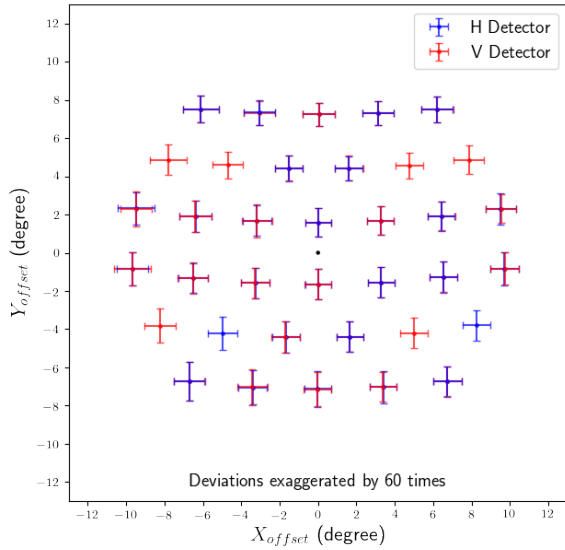


Figure 4. CLASS 40 GHz telescope array pointing overview. Detectors sensitive to ± 45 degrees polarization are shown in blue (red) data points. The displayed standard deviations are inflated by a factor of 60, i.e. one degree in the error bar is actually one arcmin. The array pointing center is indicated by a black dot.

to reveal potential side lobes. However, no unexpected side lobes are visible in the beam map.

To measure the radial profile, data points are binned within annuli with 0.05° width. The profile is estimated from the medians within each annulus, with uncertainties estimated as the standard errors. The radial profile, along with its uncer-

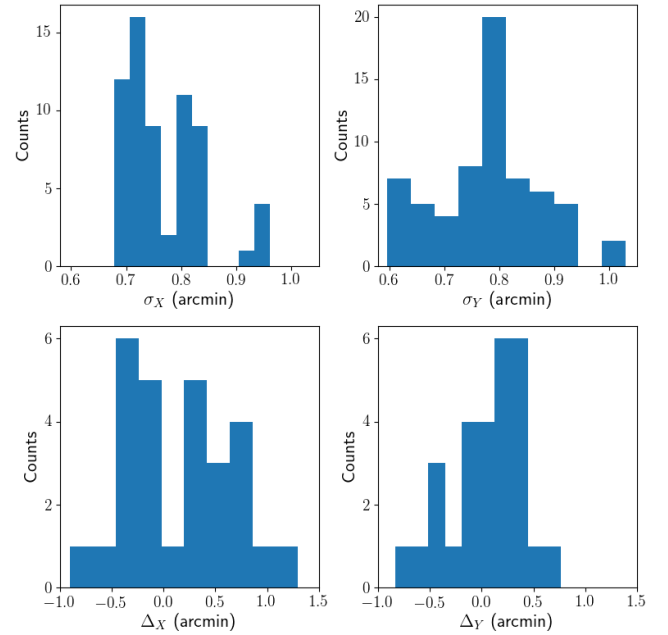


Figure 5. Pointing parameter histogram. Standard deviations (denoted as σ_X and σ_Y) are shown in top two plots with the same x-scale. Differential pointing (denoted as Δ_X and Δ_Y) are shown in bottom two plots.

tainties, shows that the profile follows the optical model for signals > -30 dB and is signal dominated to $\sim 7^\circ$. The noise level is at ~ -50 dB level except for the central region for two reasons. First, the steepness of the profile in the central region leads to a significant gradient within a finite-width annulus; and second, the ellipticity of the beam leads to data points within a circular annulus having larger standard devi-

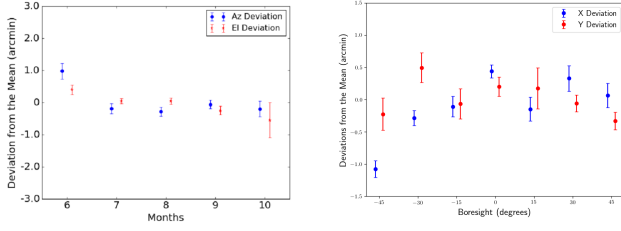


Figure 6. Pointing dependence on time and boresight angle for one typical detector. Blue (red) points show pointing deviations from the overall mean along the X (Y) direction. The blue and red points are offset from the same x values for clarity. The error bars are standard errors within the corresponding sub-sample. *Left:* Pointing dependence on time. The pointing is stable within 1 arcmin (1 % of the beam FWHM) over multiple months. *Right:* Pointing dependence on boresight angles. The trend and amplitude (~ 1 arcmin) of the azimuth deviation is consistent the estimation from our mechanical design.

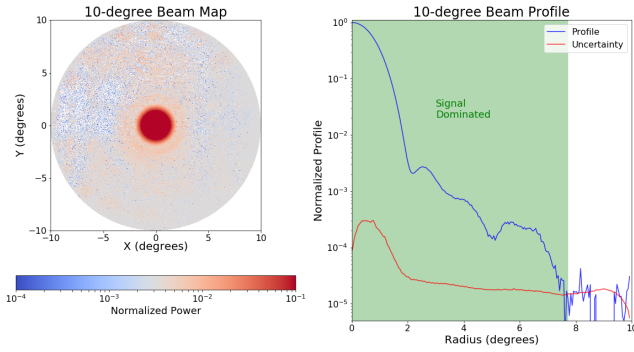


Figure 7. A typical beam map is shown on the left. The color scale is logarithmic from 10^{-1} to 10^{-4} (normalized at the peak). This scale is selected to reveal any possible side lobes. On the right, the radial profile is measured in 0.05° annuli from the beam map, shown in blue curve. Uncertainties, shown in red curve, are estimated from the standard error of data points within each annulus. The green-shaded area shows the signal-dominated region within a 7° radius.

This figure is outdated and inappropriate for publication. It can just be treated as a placeholder.

ations. Once outside of the central region, the uncertainty is at ~ -50 dB level, providing a 50 dB measurement of the intensity beam map, as estimated in Section 3.1. Beam maps across the array share the same properties as discussed above.

Once high-fidelity beam maps are available, characteristic parameters are measured. Both the stacked beam maps and single-scan beam maps are fitted by a 2-D Gaussian profile. Full width at half maximum (FWHM) is then measured along the major-axis and minor-axis. Ellipticity is calculated as $(a-b)/a$,

The definition may need to be revisited.

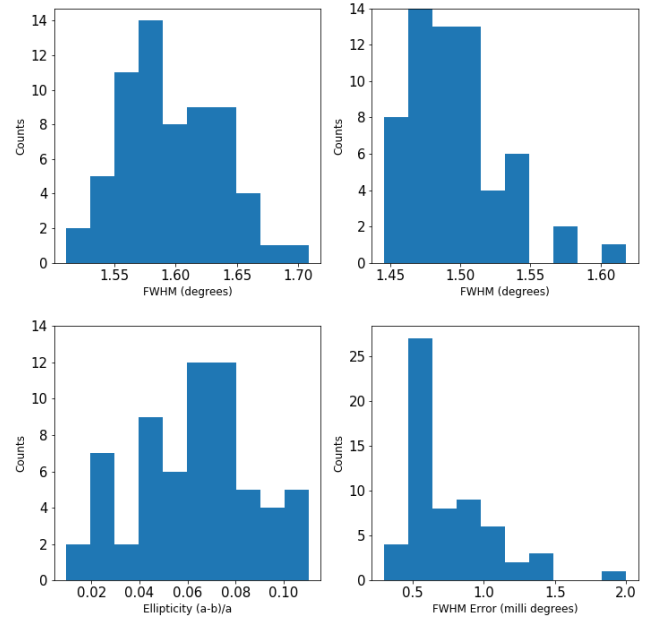


Figure 8. The histogram of beam parameters across all detectors. Histograms of major-axis and minor-axis FWHMs are shown on the top. Ellipticity is shown on the bottom left. Uncertainty of the FWHM measurement (estimated from different Moon scans) is shown on bottom right.

where a and b are the semi-major axis and semi-minor axis. Since FWHM measurements could be made from individual Moon scans, the standard error estimates the uncertainty. The major-axis FWHM and the minor-axis FWHM are treated separately for each detector.

Figure 8 shows histograms of the major-axis FWHM, the minor-axis FWHM, the ellipticity, and the uncertainty on FWHM measurement. Both the major-axis and minor-axis FWHMs are distributed within a 0.2° range, with the major-axis FWHM centering around 1.58° and the minor-axis FWHM centering around 1.48° . Since the beam maps are convolved with the Moon; the measured FWHM is enlarged by $\sim 0.03^\circ$.

Work with Bastian to see whether we can provide Moon-deconvolved results directly.

Therefore, the FWHM measurements across different detectors can be summarized as 1.55° (major-axis) and 1.45° (minor-axis), with around 0.05° deviations across the array. The average of the two FWHMs is 1.5° , as expected from the optical design. Beam ellipticity is shown to be within 0.1, centering at around 0.07. Although FWHMs across different detectors vary at the 0.1° level, the FWHM measurement for a single detector is accurate to the 0.001° level. Figure 8 on the bottom right shows the estimated uncertainties for FWHM measurements. The majority have $< 0.001^\circ$ error, peaking at around 0.0005° . The FWHM measurement uncertainties are much smaller than the difference between major-axis FWHMs and minor-axis

FWHMs ($\sim 0.1^\circ$), demonstrating the beam ellipticity is from the instrument.

Cautious about saying this.

For cosmological analyses, beams on the sky will be averaged across boresight angles. With even coverage across 90° boresight angles (rotating major axis to minor axis), ellipticity is averaged out for cosmological beams.

Show some cosmology beams? How deep do we get into this?

7. MOON TEMPERATURE MODEL

A measured moon map, \tilde{T} , can be modeled as the convolution between the moon as uniform disc T with an angular radius a , and a symmetric beam, B :

$$\tilde{T} = T * B + N, \quad (3)$$

where a small noise component N was added.

This convolution can be represented in the k -domain by applying the Fourier projector $\mathcal{F}^{-1}(\mathcal{F}(\cdot))$ and using the Fourier representation of the uniform disc, $2\pi a^2 J_1(ka)/ka$ with $J_1(x)$ the Bessel function of the first kind; thus,

$$\tilde{T}(\theta, \phi) = \frac{a}{(2\pi)} \int_{\mathbb{R}^2} d\mathbf{k} e^{i\mathbf{k} \cdot \mathbf{x}} \frac{J_1(ka)}{k} B(k) + N(\theta, \phi). \quad (4)$$

It is suitable to use the rotational symmetry of the convolved signal by doing the following substitutions: $x = \theta \cos \phi$, $y = \theta \sin \phi$; the identity $\cos \xi \cos \phi + \sin \xi \sin \phi = \cos(\xi - \phi)$; and making a change of variables $\xi - \phi = \psi$. In this formulation, the radial temperature distribution becomes:

$$\tilde{T}(\theta, \phi) = \frac{a}{(2\pi)} \int_0^\infty \int_0^{2\pi} dk d\psi e^{ik\theta \cos \psi} J_1(ka) B(k) + N(\theta, \phi). \quad (5)$$

Additionally, by using the integral representation of the zeroth order Bessel function of the first kind, $2\pi J_0(z) = \int_0^{2\pi} d\psi e^{\pm iz \cos \psi}$, and taking the angular average of the noise $\langle N(\theta, \phi) \rangle_\phi = N(\theta)$, the observed temperature map can be re-expressed as a function of only θ :

$$\tilde{T}(\theta) = 2\pi a \int_0^\infty dk J_0(k\theta) J_1(ka) B_0(k) + N(\theta), \quad (6)$$

where $B_0(k)$ is the zeroth Hankel transform of the beam defined by $B_0(k) = \int_0^\infty d\theta \theta B(\theta) J_0(k\theta)$.

The above analytical expression is the model of the moon-beam convolution. Notice that it has been reduced from 2-dimensional convolution (two integrals) to a single integral expression by using the rotational symmetry of both functions. This reduces the fitting computation process.

7.1. Beam fitting and deconvolution

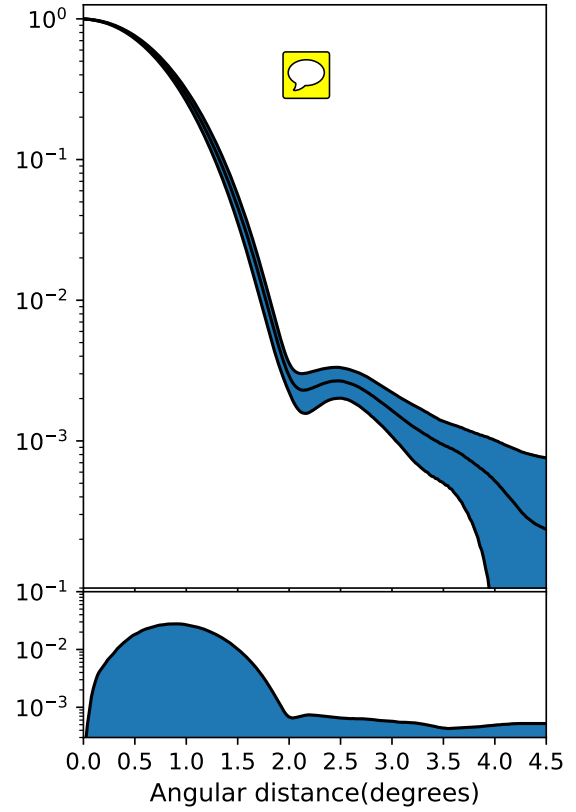


Figure 9. Average beam profile. The shaded region denotes an 1- σ of uncertainty envelope around the beam average along the season.

A symmetric beam which deviates slightly from a gaussian one can be represented as an even linear combination of Hermite modes denoted by B_j ,

$$B(\theta) = \sum_{j=0}^{N_{\max}} a_{2j} B_{2j} \left(\frac{\theta}{\sigma_b} \right), \quad (7)$$

analytically as,



$$B(\theta) = \sum_{j=0}^{N_{\max}} a_{2j} H_{2j} \left(\frac{\theta}{\sigma_b} \right) \exp \left(-\frac{1}{2} \frac{\theta^2}{\sigma_b^2} \right), \quad (8)$$

where $2j$ is an even number. This expansion allows to capture and parametrize the small features that deviates from the gaussianity. This basis has already been implemented in ref[] thus in order to obtain the beam shape from moon scans data,

A $2n$ -Hermite polynomials have a maximum at $\theta = \pm \sigma_b \sqrt{2n}$, and then they decays gaussianly, and our effective beam has its last relevant feature at ~ 4.0 (deg) which implies $[2N_{\max}] = 34$ this impose an upper limit, $N_{\max} \leq 17$, for the beam expansion.



It is useful to fit indirectly the beam shape $B(\theta)$, by defining transformed basis of the Hermite modes, $\tilde{T}_{2j}(\theta)$ as, [as the expression]

$$\tilde{T}_{2j}(\theta) = 2\pi a \int_0^\infty dk J_0(k\theta) J_1(ka) B_{0,2j}(k) \quad (9)$$

where $B_{0,2j}(k)$ is the 2D-Hankel transformation of $B_{2j}(\theta)$. Then the temperature map can be expanded linearly as,

$$\tilde{T}(\theta) = \sum_j a_{2j} \tilde{T}_{2j}(\theta) + N(\theta). \quad (10)$$

Therefore, if the coefficients set a_{2j} are found, the beam shape will be determined.

Due to we are interested only in the beam shape it is suitable normalize the map at $\theta = 0$ to the unity. If $N(0) \ll \tilde{T}(0)$

$$\hat{i}(\theta) = \frac{\int_0^\infty dk J_0(k\theta) J_1(ka) B_0(k)}{\int_0^\infty dk J_1(ka) B_0(k)} + n(\theta)$$

where: $n(\theta) = N(\theta)/\tilde{T}(0)$.

To take Hankel transform of a even Hermite function, is better expand the function in its components (eq.) and take the Hankel transform to each of them, and then proceed with its reconstruction in Fourier space.

Because of the fact that the only is composed by even order polynomials $\left(\frac{\theta}{\sigma_b}\right)^{2n} \exp\left(-\frac{\theta^2}{2\sigma_b^2}\right) \subseteq B_{2n}(\theta) = H_{2n}\left(\frac{\theta}{\sigma_b}\right) \exp\left(-\frac{1}{2} \frac{\theta^2}{\sigma_b^2}\right)$ then in function to get the Hankel transform of the different Hermite modes, first it is better obtain the Hankel transform of the even components of a Hermite mode and then reconstruct them in Fourier space. For the even components, their Hankel transform is given by:

$$\mathcal{H}_0 \left[\left(\frac{\theta}{\sigma_b} \right)^{2n} \exp \left(-\frac{\theta^2}{2\sigma_b^2} \right) \right] (k) = 2^n \sigma_b^2 \Gamma(n+1) \cdot {}_1F_1 \left(n+1; 1; -\frac{\sigma_b^2 k^2}{2} \right)$$

where ${}_1F_1(a, b, z)$ are the confluent hypergeometric functions of the first kind. This allows to obtain an analytical expression in Fourier representation for different Hermite modes, as a consequence, each component of the convolved basis, $\tilde{T}_{2j}(\theta)$, is determined exactly as an integral representation of known functions. So one can obtain [eq.]

Returning to eq. and by (above result) using the convolved Hermite basis, the normalized moon-beam model [eq.] can be expanded in terms of the components of this basis.

$$\hat{i}(\theta) = \frac{\sum_{j=0}^{N_{\max}} a_{2j} \tilde{T}_{2j}(\theta)}{\sum_{j=0}^{N_{\max}} a_{2j} \tilde{T}_{2j}(0)} + n(\theta)$$

The above expression is conformally symmetric under a rescaling transformation $\tilde{T} \rightarrow a\tilde{T}$, therefore to avoid a scale degeneracy in the set coefficient $\{a_{2n}\}$, it is suitable choose one of them to unity, for instance a_{0j} thus

$$\hat{i}(\theta) = \frac{\tilde{T}_0(\theta) + \sum_{j=1}^{N_{\max}} \hat{a}_{2j} \tilde{T}_{2j}(\theta)}{\tilde{T}_0(0) + \sum_{j=1}^{N_{\max}} \hat{a}_{2j} \tilde{T}_{2j}(0)} + n(\theta)$$

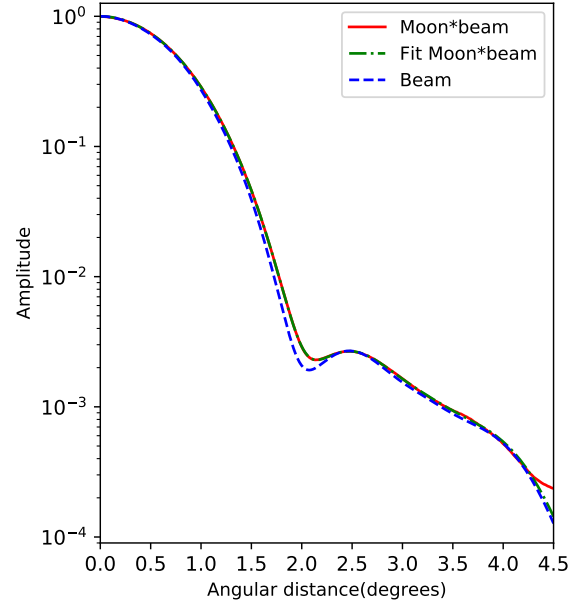


Figure 10. Beam profile

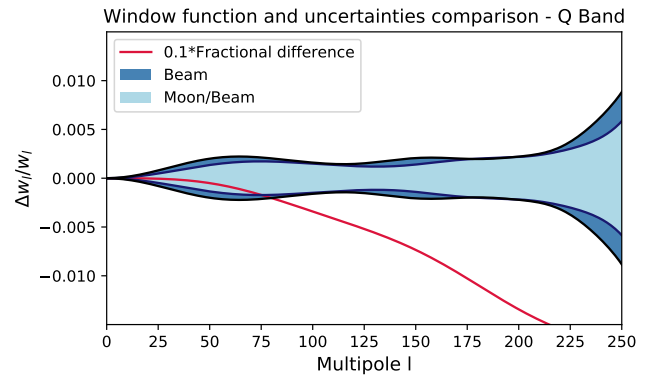


Figure 11. khsbchb

8. WINDOW FUNCTION

8.1. Beam response function

For a solid angle normalized azimuthally symmetric beam $b(\theta)$, its harmonic representation is reduced to

$$b_l^T = \int d\Omega b(\theta) P_l(\cos \theta) \quad (11)$$

Table 2. Window function parameters

Parameter	February	August
$\sigma_b(\text{deg})$	$0.67 \pm 1.04 \cdot 10^{-6}$	$0.66 \pm 6.81 \cdot 10^{-6}$
$FWHM(\text{deg})$	$1.57 \pm 2.46 \cdot 10^{-6}$	$1.56 \pm 1.60 \cdot 10^{-6}$
$\Omega_b(10^{-4}\text{rad}^2)$	8.08 ± 0.02	7.90 ± 0.01
$l^{b=0.5}$	~ 110	~ 110
$l^{b=0.2}$	~ 165	~ 165
N_{max}	12	12
l_{max}	~ 225	~ 225



additionally, For a perfectly co-polar beam the and assuming fully polarized detectors, with no sensitivity to circular polarization

the beam Q and U Stokes parameter can be obtained from

$$Q_b \pm iU_b = -b(\theta)e^{\pm 2i\phi} \quad (12)$$

as a spin-2 field can be represented in spherical harmonic of spin-2, $_{\pm 2}Y_{lm}$, whose harmonic representation, for a fully azimuthally symmetric beam[Fosalba], its harmonic spin-2 representation reduces to

$$b_l^P = -(4\pi) \frac{(l-2)!}{(l+2)!} \int d\theta \sin\theta b(\theta) {}_{-2}P_l^2(\cos\theta) \quad (13)$$

where the superscripts label $P = E, B$.

8.2. Windows functions

Cross window function

$$w_l^{ij} = b_l^i b_l^j \quad (14)$$

with $i, j = T, E$ or B

[Gary paper] for uncertainty propagation.

8.3. Uncertainties propagation

$$\Delta b_l^i = b_l^i(\bar{a}) - \langle b_l^i \rangle = \sum_{n=0}^N \frac{\partial b_l^i}{\partial a_n} (a_n - \langle a_n \rangle) \quad (15)$$

the beam covariance matrix is then defined:

$$\Sigma_{b, ll'}^{ij} = \langle \Delta b_l^i \Delta b_{l'}^j \rangle \quad (16)$$

$$\Sigma_{b, ll'}^{ij} = \sum_{n, n'} \frac{\partial b_l^i}{\partial a_n} \langle (a_n - \langle a_n \rangle)(a_{n'} - \langle a_{n'} \rangle) \rangle \frac{\partial b_{l'}^j}{\partial a_{n'}} \quad (17)$$

$$\Sigma_{ll'}^{ij} = \sum_{n, n'} \frac{\partial b_l^i}{\partial a_n} \Sigma_{nn'}^{aa} \frac{\partial b_{l'}^j}{\partial a_{n'}} \quad (18)$$

for the beam response function normalized to the solid angle $b_l^i = B_l^i / B_{l=0}^T$. After some algebra one arrives to:

$$\Sigma_{ll'}^{ij} = \frac{1}{(B_{l=0}^T)^2} \left[\Sigma_{B, ll'}^{ij} + b_l^i b_{l'}^j \Sigma_{B, 00}^{TT} - b_l^i \Sigma_{B, 0l'}^{Tj} - b_{l'}^j \Sigma_{B, l0}^{iT} \right] \quad (19)$$

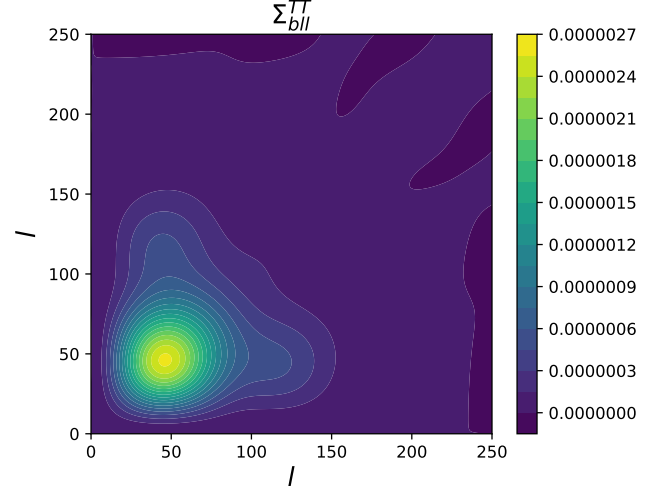


Figure 12. Temperature-temperature beam covariance matrix in harmonic representation.

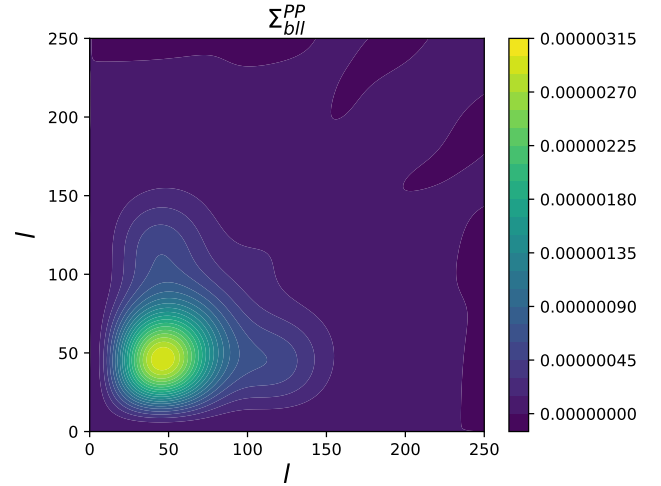


Figure 13. Polarization-polarization beam covariance matrix in harmonic representation.

9. MOON POLARIZATION MAP

As discussed in Section 3.1, Moon polarization signal is estimated to be around three orders of magnitude lower than the intensity signal, similar to the ratio of the CMB temperature fluctuations to polarization fluctuations. Therefore, demonstrating polarization signal can be isolated at this level

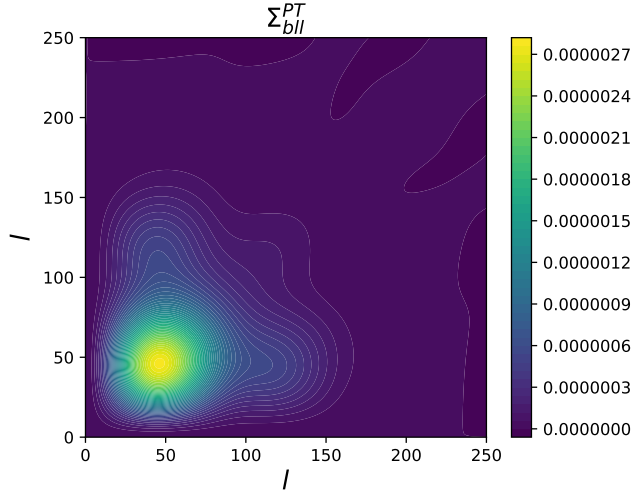


Figure 14. Polarization-temperature beam covariance matrix in harmonic representation.

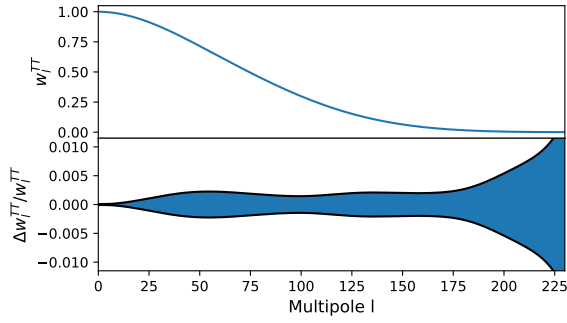


Figure 15. Temperature-temperature window function.

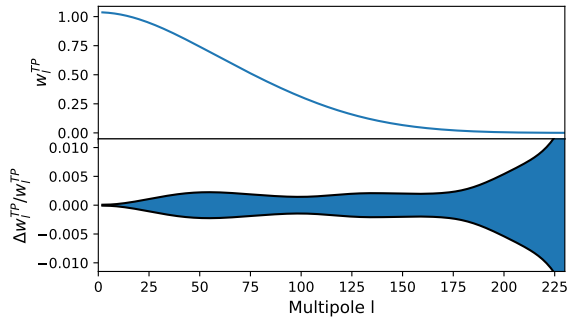


Figure 16. Temperature-polarization window function. P = E,B

indicates that the CMB polarization signal can also be isolated for cosmological studies.

The variable-delay polarization modulator (VPM) modulates incoming polarization signal. The polarization signal is then extracted from the modulated raw data, called demodulation. Details can be found in a companion paper ([cite Katie's paper](#)). After the Moon scan data are demodulated,

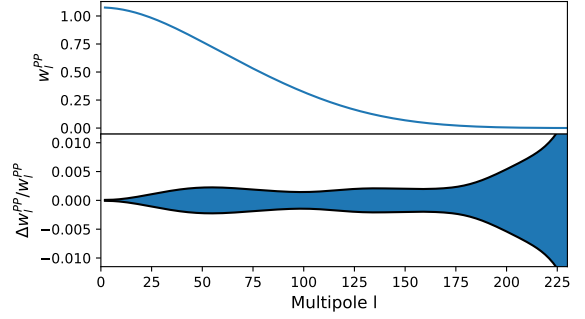


Figure 17. Polarization-polarization window function. P = E,B

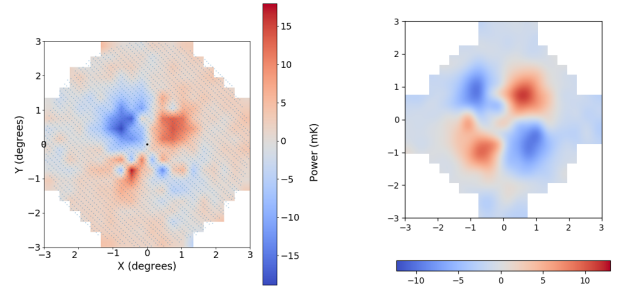


Figure 18. Moon polarization maps for one typical detector pair. Result from one Moon scan is shown on the left, while stacked result is shown on the right. *Left:* Quadrupole patterns are visible for one Moon scan, with amplitudes of 10 ~ 20 mK. The uneven power is due to the uneven temperature of the Moon regolith. *Right:* The stacked map shows higher signal-to-noise with the similar amplitude. Since the stacked Moon maps were observed during different phase of the Moon, the power unevenness averages down.

This plot definitely needs to be re-made.

beam maps are generated similar to the intensity ones, but for polarization signals.

9.1. Single Detector

Naturally, we should talk about polarized moon maps for individual detectors. But I don't think we understand the dipoles in them. I see this become a priority to understand the instrument.

9.2. Pair Differencing

Moon polarization maps from one detector pair were added together, equivalent to pair differencing. Before performing pair differencing, gains between paired detectors were balanced to remove temperature-to-polarization leakage. These procedures were all performed in time-ordered data (TOD) space.

Quadrupole patterns (similar to that in Figure 2) emerged across the array. Figure 18 shows the quadrupole pattern for one typical detector pair. Amplitude of the pattern is 10 ~ 20 mK, around three orders of magnitude lower than the intensity amplitude, consistent with our simulation results

(Section 3.1). The uneven power is due to the uneven tempration of the Moon regolith, as discussed in Section 3.1. Stacking maps across different Moon scans provides higher signal-to-noise result, also averages down the power unevenness as the stacked Moon scans were observed during different phases of the Moon.

Real simulations with the correct orientation of the Moon on the sky should be presented for each Moon scan, this will help us verifying the uneven pattern we measure, and also help us with the polarization angle determination later.

9.3. Polarization Angle Determination

The circular symmetry of the Moon polarization pattern could be used to determine the telescope far-field polarization angle via the orientation of quadrupole patterns. An effective tool to extract quadrupole components in the polarization beam maps is Gauss-Hermite patterns. Gauss-Hermite patterns form a complete and orthogonal basis for a 2-D space (Essinger-Hileman et al. 2016), with an analytical expression

$$f_{i,j}(\theta, \phi) = \left(\frac{\exp[-\theta^2/(2\sigma^2)]}{\sqrt{2^{i+j}i!j!\pi\sigma^2}} \right) \times H_i\left(\frac{\theta \cos \phi}{\sigma}\right) H_j\left(\frac{\theta \sin \phi}{\sigma}\right), \quad (20)$$

where θ and ϕ describe the map in polar coordinate system, H_i and H_j are Hermite polynomials, and $\sigma = \text{FWHM}/\sqrt{8 \ln 2}$ is the Gaussian width of the beam.

Basic Gauss-Hermite patterns are shown in Figure 19. The two orthogonal quadrupole patterns are rotated 45° relative to each other. Ratio of the two patterns determines the orientation of the combined quadrupole pattern. The completeness and orthogonality of Gauss-Hermite patterns guarantees that all quadrupole information is and only is stored within these two patterns.

Each polarization beam map was fitted with the Gauss-Hermite patterns up to order of 10, meaning $i+j \leq 10$. Beyond order 10, negligible improvement is achieved. The quadrupole patterns are then recovered with fitted coefficients on the two orthogonal Gauss-Hermite quadrupole patterns. The polarization angles were then calculated from the two coefficients, which informs the far-field telescope polarization angle. Figure 20 presents the result for one typical detector.

10. OPTICAL MODELING & SIMULATION

10.1. Simulations

We used GRASP (kk add reference) to investigate the electromagnetic properties of CLASS Q-band receiver. Simulations were carried out in *hades*, a 64 AMD Opteron core and 128 GB of RAM computing node at Centro de Astroingenieria UC. The model includes the reimaging optics, window, reflective optics, closeout, the cage, and the forebaffle. All

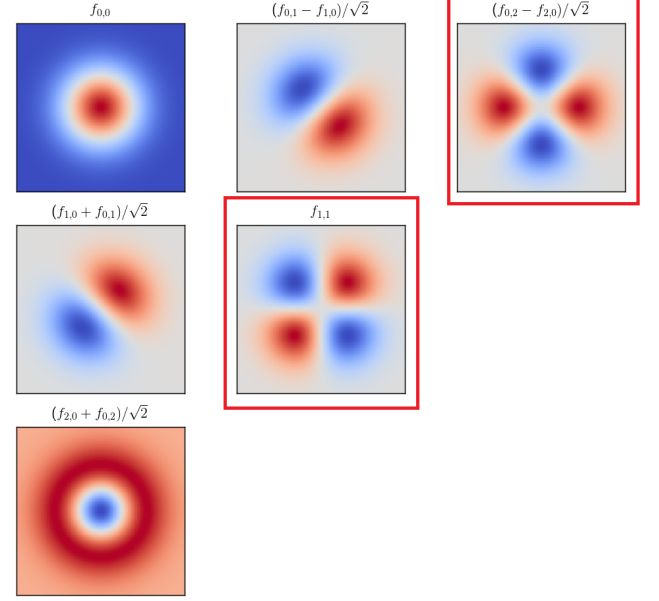


Figure 19. Basic Gauss-Hermite patterns are shown with $f_{i,j}$ defined in Equation 20. The two quadrupole components are pointed out with red boxes. $i+j$ is defined as the order of the function.

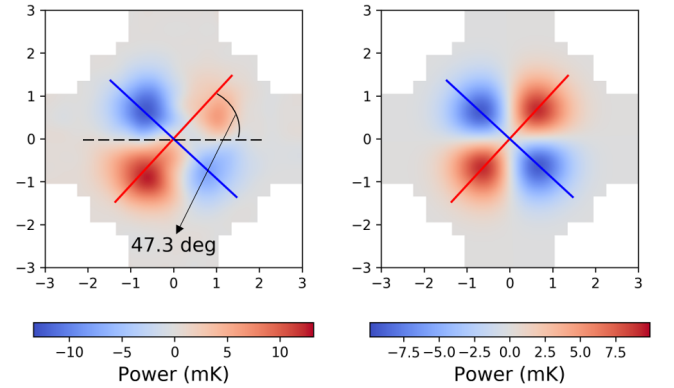


Figure 20. Polarization angle determination. A measured Moon polarization map is shown on the left, with the extracted quadrupole component shown on the right. The polarization angle is determined as 47.6° from the Gauss-Hermite separation method. Auxiliary lines are plotted representing the orientation of the quadrupole pattern.

reflective elements are perfectly conducting, zero roughness surfaces. Screen captures of the model are shown in figure 21.

Infrared filters were not included in the model as they are too close to each other, causing the Physical Optics approximation to give unreliable results. Using a plane-wave expansion to compute the fields of nearby surfaces is possible, but implementing this for all 72 detectors increases the complexity of the model significantly. The Variable delay Polarization Modulator (VPM) was modelled as a single circular, flat

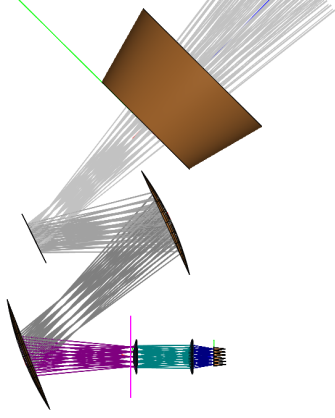


Figure 21. Screen capture of the GRASP model used for to simulate the CLASS Q-band receiver. The ray trace for all detectors is shown in different colours as they traverse the different optical components.

mirror. This is because the VPM alone is a complex electromagnetic system that requires detailed modelling which, if included in the complete CLASS GRASP model, would make the computation exceed the machine’s capabilities.

We used Physical Optics simulations on the CLASS Q-band receive to study first order effects in the beam, like eccentricity and cross polarization. The simulations use a Gaussian beam pattern as the beam forming element. The gaussian beam as a -10 dB taper at 14 degrees away from the chief ray, as described in (Zeng et al. 2010)(kk reference to Joseph’s paper). Following CLASS mechanical design, each detector is simulated by orienting the feedhorn at 45 degrees or -45 degrees fwith respect to the optical plane. GRASP then computes the optical chain by propagating the fields from one element to the next, computing the currents at the surface of the element using the Physical Optics approximation. Mirror and aperture edges are treated using GRASP’s implementation of the Physical Theory of Diffraction (PTD) (Keller 1962). The optical chain starts at the feedhorns and ends at the telescope closeout (kk include a diagram that shows what is what in the model) At the closeout, a plane wave expansion of the currents is computed, which is then used to illuminate the inside region of the forebaffle. This is because the closeout is too close to the walls of the forebaffle to that the PO approximation does not hold (TICRA, private communication). The fields from this plane wave expansion

illuminate the inner walls of the forebaffle, whose currents are computed using Bor-MoM, an accelerated version of the Method of Moments for bodies of revolution (kk reference to this). Finally, the currents from the closeout and the forebaffle are projected into a 5×5 degree alt-az grid, such that the beam map obtained from the field projection is equivalent to the observation of a point source at zero degrees elevation. An example of a beam obtained from this procedure is shown in figure ...

10.2. Comparison of GRASP simulations with Moon observations

To validate the optical simulations, we made GRASP simulations for all the detectors of the CLASS Q-band receiver. The GRASP simulations used for this comparison do not include the effect of the forebaffle, which significantly increases the computational effort from 15 seconds to 20 minutes per detector. (kk argue that baffle spill over is low, etc)

The comparison is made by first normalizing the GRASP beams to their maxima so that the beam peak is equal to 1. As GRASP outputs electric fields in the far field, so the normalized beam power must be computed as

$$B_g = \frac{\vec{E}_{co}\vec{E}_{co}^* + \vec{E}_{cx}\vec{E}_{cx}^*}{\max[\vec{E}_{co}\vec{E}_{co}^* + \vec{E}_{cx}\vec{E}_{cx}^*]} \quad (21)$$

where \vec{E}_{co} and \vec{E}_{cx} are the CO and Cross polar components of the electric field in the far field.

Secondly, we must ensure that the GRASP and Moon map grids are aligned correctly. GRASP evaluates the electric fields on an alt-az grid centered on a vector pointing with some on-sky offset angles with respect to the boresight pointing. The simulations use the nominal pointing solution of CLASS as a starting point to position the field evaluation grids on the sky. We the evaluation grids positioned this way suffer from a systematic offset. To correct for this effect, we iterated on the optical simulations by computing the offsets from the nominal pointing solution and then correcting the position of the field evaluation grids. This ensures that all beam maps obtained from GRASP simulations will have its maximum at the center of the evaluation grid.

11. FAR SIDE LOBES

I do want to look into this. I am planning on making some sun-centered maps to start.

REFERENCES

- A. A. Penzias and R. W. Wilson. A Measurement of Excess Antenna Temperature at 4080 Mc/s. *ApJ*, 142:419–421, July 1965. doi:10.1086/148307. 1
- D. J. Fixsen, E. S. Cheng, J. M. Gales, J. C. Mather, R. A. Shafer, and E. L. Wright. The Cosmic Microwave Background Spectrum from the Full COBE FIRAS Data Set. *ApJ*, 473:576, December 1996. doi:10.1086/178173. 1
- C. L. Bennett, A. J. Banday, K. M. Gorski, G. Hinshaw, P. Jackson, P. Keegstra, A. Kogut, G. F. Smoot, D. T. Wilkinson, and E. L. Wright. Four-Year COBE DMR Cosmic Microwave Background Observations: Maps and Basic Results. *ApJL*, 464: L1, June 1996. doi:10.1086/310075. 1

- G. Hinshaw, D. Larson, E. Komatsu, D. N. Spergel, C. L. Bennett, J. Dunkley, M. R. Nolta, M. Halpern, R. S. Hill, N. Odegard, L. Page, K. M. Smith, J. L. Weiland, B. Gold, N. Jarosik, A. Kogut, M. Limon, S. S. Meyer, G. S. Tucker, E. Wollack, and E. L. Wright. Nine-year Wilkinson Microwave Anisotropy Probe (WMAP) Observations: Cosmological Parameter Results. *ApJS*, 208:19, October 2013. doi:10.1088/0067-0049/208/2/19. [1](#)
- Planck Collaboration, P. A. R. Ade, N. Aghanim, M. Arnaud, M. Ashdown, J. Aumont, C. Baccigalupi, A. J. Banday, R. B. Barreiro, J. G. Bartlett, and et al. Planck 2015 results. XIII. Cosmological parameters. *A&A*, 594:A13, September 2016. doi:10.1051/0004-6361/201525830. [1](#)
- M. Kamionkowski, A. Kosowsky, and A. Stebbins. A Probe of Primordial Gravity Waves and Vorticity. *Physical Review Letters*, 78:2058–2061, March 1997. doi:10.1103/PhysRevLett.78.2058. [1](#)
- U. Seljak and M. Zaldarriaga. Signature of Gravity Waves in the Polarization of the Microwave Background. *Physical Review Letters*, 78:2054–2057, March 1997. doi:10.1103/PhysRevLett.78.2054. [1](#)
- Duncan J. Watts, Bingjie Wang, Aamir Ali, John W. Appel, Charles L. Bennett, David T. Chuss, Sumit Dahal, Joseph R. Eimer, Thomas Essinger-Hileman, Kathleen Harrington, Gary Hinshaw, Jeffrey Iuliano, Tobias A. Marriage, Nathan J. Miller, Ivan L. Padilla, Lucas Parker, Matthew Petroff, Karwan Rostem, Edward J. Wollack, and Zhilei Xu. A projected estimate of the reionization optical depth using the CLASS experiment’s sample variance limited e-mode measurement. *The Astrophysical Journal*, 863(2):121, aug 2018. doi:10.3847/1538-4357/aad283. URL <https://doi.org/10.3847/1538-4357/aad283>. [1](#)
- R. Allison, P. Caucal, E. Calabrese, J. Dunkley, and T. Louis. Towards a cosmological neutrino mass detection. *Phys. Rev. D*, 92:123535, Dec 2015. doi:10.1103/PhysRevD.92.123535. URL <https://link.aps.org/doi/10.1103/PhysRevD.92.123535>. [1](#)
- J. W. Appel, A. Ali, M. Amiri, D. Araujo, C. L. Bennet, F. Boone, M. Chan, H.-M. Cho, D. T. Chuss, F. Colazo, E. Crowe, K. Denis, R. Dünner, J. Eimer, T. Essinger-Hileman, D. Gothe, M. Halpern, K. Harrington, G. Hilton, G. F. Hinshaw, C. Huang, K. Irwin, G. Jones, J. Karakula, A. J. Kogut, D. Larson, M. Limon, L. Lowry, T. Marriage, N. Mehrle, A. D. Miller, N. Miller, S. H. Moseley, G. Novak, C. Reintsema, K. Rostem, T. Stevenson, D. Towner, K. U-Yen, E. Wagner, D. Watts, E. Wollack, Z. Xu, and L. Zeng. The cosmology large angular scale surveyor (CLASS): 38-GHz detector array of bolometric polarimeters. In *Millimeter, Submillimeter, and Far-Infrared Detectors and Instrumentation for Astronomy VII*, volume 9153 of *Proc. SPIE*, page 91531J, July 2014. doi:10.1117/12.2056530. [2](#), [3](#)
- J. R. Eimer, C. L. Bennett, D. T. Chuss, T. Marriage, E. J. Wollack, and L. Zeng. The cosmology large angular scale surveyor (CLASS): 40 GHz optical design. In *Millimeter, Submillimeter, and Far-Infrared Detectors and Instrumentation for Astronomy VI*, volume 8452 of *Proc. SPIE*, page 845220, September 2012. doi:10.1117/12.925464. [2](#), [3](#), [1](#)
- Y. C. Zheng, K. T. Tsang, K. L. Chan, Y. L. Zou, F. Zhang, and Z. Y. Ouyang. First microwave map of the Moon with Chang’E-1 data: The role of local time in global imaging. *Icarus*, 219:194–210, May 2012. doi:10.1016/j.icarus.2012.02.017. [3.1](#), [2](#)
- X.-Z. Zhang, A. Gray, Y. Su, J.-D. Li, T. Landecker, H.-B. Zhang, and C.-L. Li. New radio observations of the Moon at L band. *Research in Astronomy and Astrophysics*, 12:1297–1312, September 2012. doi:10.1088/1674-4527/12/9/010. [3.1](#)
- T. Essinger-Hileman, A. Kusaka, J. W. Appel, S. K. Choi, K. Crowley, S. P. Ho, N. Jarosik, L. A. Page, L. P. Parker, S. Raghunathan, S. M. Simon, S. T. Staggs, and K. Visnjic. Systematic effects from an ambient-temperature, continuously rotating half-wave plate. *Review of Scientific Instruments*, 87(9):094503, September 2016. doi:10.1063/1.4962023. [9.3](#)
- L. Zeng, C. L. Bennett, D. T. Chuss, and E. J. Wollack. A low cross-polarization smooth-walled horn with improved bandwidth. *IEEE Transactions on Antennas and Propagation*, 58(4):1383–1387, April 2010. ISSN 0018-926X. doi:10.1109/TAP.2010.2041318. [21](#)
- Joseph B. Keller. Geometrical theory of diffraction*. *J. Opt. Soc. Am.*, 52(2):116–130, Feb 1962. doi:10.1364/JOSA.52.000116. URL <http://www.osapublishing.org/abstract.cfm?URI=josa-52-2-116>. [21](#)

APPENDIX

A. BEAM CONVENTIONS

Normalized to unity beam, $B(\theta)$, is such that $B(0) = 1$

Solid angle:

$$\Omega_B = \int d\Omega B(\theta) \quad (A1)$$

Solid angle normalized beam

$$b(\theta) = B(\theta)/\Omega_B \quad (A2)$$

A.1. Mathematical tools

The spherical Harmonics are defined as:

$$Y_{lm}(\theta, \phi) = N_{lm} P_l^m(\cos \theta) e^{im\phi} \quad (A3)$$

with:

$$N_{lm} = \sqrt{\frac{(2l+1)}{4\pi}} \sqrt{\frac{(l-m)!}{(l+m)!}} \quad (A4)$$

where P_l^m are the associated Legendre polynomials.

Addition theorem:

$$P_l(\hat{x} \cdot \hat{y}) = \frac{4\pi}{(2l+1)} \sum_{m=-l}^{m=l} Y_{lm}(\hat{x}) Y_{lm}^*(\hat{y}) \quad (A5)$$

where \hat{x} and \hat{y} are units vectors.

For different multipolar expansion along this notes is understood that:

$$\sum_{l=0}^{\infty} \sum_{m=-l}^{m=l} \rightarrow \sum_l \sum_m \quad (A6)$$

B. BEAM RESPONSE

A temperature map is obtained projecting into the spherical harmonic basis:

$$T(\theta, \phi) = \sum_{lm} T_{lm} Y_{lm}(\theta, \phi) \quad (B7)$$

or compactly in a coordinate free way.

$$|T\rangle = \sum_{lm} T_{lm} |lm\rangle \quad (B8)$$

,analogously the beam function, which is mathematically is a kernel can be writting in a coordinate free manner, defining the beam operator:

$$\hat{b} = \sum_{l_1 l_2} \sum_{m_1 m_2} b_{l_2 m_2 l_1 m_1} |l_2 m_2\rangle \langle l_1 m_1| \quad (B9)$$

in real space representation:

$$b(\hat{n}_2, \hat{n}_1) = \sum_{l_1 l_2} \sum_{m_1 m_2} b_{l_2 m_2 l_1 m_1} Y_{l_2 m_2}^*(\hat{n}_2) Y_{l_1 m_1}(\hat{n}_1) \quad (B10)$$

The coordinate free representation is clearer than real space convolution, but the real space convolution is more intuitive, for example a convolution is:

$$|\tilde{T}\rangle = \hat{b}|T\rangle \quad (\text{B11})$$

$$= \sum_{l_1 l_2} \sum_{m_1 m_2} b_{l_2 m_2 l_1 m_1} T_{l_1 m_1} |l_2 m_2\rangle \quad (\text{B12})$$

$$(\text{B13})$$

projecting in the real basis:

$$\tilde{T}(\hat{n}_2) = \sum_{l_1 l_2} \sum_{m_1 m_2} b_{l_2 m_2 l_1 m_1} T_{l_1 m_1} Y_{l_2 m_2}(\hat{n}_2) \quad (\text{B14})$$

which is equivalent to:

$$\tilde{T}(\hat{n}_2) = \int d\Omega_1 b(\hat{n}_2, \hat{n}_1) T(\hat{n}_1) \quad (\text{B15})$$

we can identify easily the measured map coefficient $\tilde{T}_{l_2 m_2}$ as:

$$\tilde{T}_{l_2 m_2} = \sum_{l_1 m_1} b_{l_2 m_2 l_1 m_1} T_{l_1 m_1} \quad (\text{B16})$$

with this definition it easy to compute the power spectrum for temperature $\langle \tilde{T} | \tilde{T} \rangle$:

$$\langle \tilde{T} | \tilde{T} \rangle = \sum_{l'_2 l'_1} \sum_{m'_2 m'_1} \tilde{T}_{l'_2 m'_2} T_{l_2 m_2} \langle l'_2 m'_2 | l_2 m_2 \rangle \quad (\text{B17})$$

$$= \sum_{l'_2 m'_2} (\tilde{T}_{l'_2 m'_2} T_{l_2 m_2}) \quad (\text{B18})$$

$$= \sum_{l'_2 m'_2} \left(\sum_{l'_1 l_1} \sum_{m'_1 m_1} b_{l'_2 m'_2 l'_1 m'_1}^* b_{l_2 m_2 l_1 m_1} T_{l'_1 m'_1} T_{l_1 m_1} \right) \quad (\text{B19})$$

we identify:

$$|\tilde{T}_{l'_2 m'_2}|^2 = \sum_{l'_1 l_1} \sum_{m'_1 m_1} b_{l'_2 m'_2 l'_1 m'_1}^* b_{l_2 m_2 l_1 m_1} T_{l'_1 m'_1} T_{l_1 m_1} \quad (\text{B20})$$

taking the ensemble average:

$$\langle |\tilde{T}_{l'_2 m'_2}|^2 \rangle = \sum_{l'_1 l_1} \sum_{m'_1 m_1} b_{l'_2 m'_2 l'_1 m'_1}^* b_{l_2 m_2 l_1 m_1} \langle T_{l'_1 m'_1} T_{l_1 m_1} \rangle \quad (\text{B21})$$

$$\tilde{C}_{l'_2} = \sum_{l'_1 l_1} \sum_{m'_1 m_1} b_{l'_2 m'_2 l'_1 m'_1}^* b_{l_2 m_2 l_1 m_1} C_{l'_1} \delta_{l'_1 l_1} \delta_{m'_1 m_1} \quad (\text{B22})$$

$$\tilde{C}_{l'_2 m'_2} = \sum_{l'_1} \sum_{m'_1} |b_{l'_2 m'_2 l'_1 m'_1}|^2 C_{l'_1} \quad (\text{B23})$$

$$(\text{B24})$$

Noticed that beam asymmetries induce m -dependence for the measured angular power spectrum $\tilde{C}_{l' m'}$. additionally we can take the average over m and relabelling,

$$\langle \tilde{C}_{l'} \rangle = \sum_l \frac{1}{(2l+1)} \sum_{mm'} |b_{l' m' l m}|^2 \langle C_l \rangle \quad (\text{B25})$$

$$\langle \tilde{C}_{l'} \rangle = \sum_l M_{l' l} \langle C_l \rangle \quad (\text{B26})$$

for a particular case in which matrix $M_{l'l} = w_l \delta_{l'l}$, one gets:

$$\langle \tilde{C}_{l'} \rangle = w_l \langle C_l \rangle \quad (\text{B27})$$

B.0.1. Symmetric beams

The matrix coefficient of symmetric beams:

$$b_{l_1 m_1 l_2 m_2} = b_{l_1} \delta_{l_1 l_2} \delta_{m_1 m_2} \quad (\text{B28})$$

replacing into() and projecting in the spherical coordinates:

$$b(\hat{n}_2, \hat{n}_1) = \sum_{l_1 l_2} \sum_{m_1 m_2} b_{l_1} \delta_{l_1 l_2} \delta_{m_1 m_2} Y_{l_2 m_2}^*(\hat{n}_2) Y_{l_1 m_1}(\hat{n}_1) \quad (\text{B29})$$

$$= \sum_l \sum_m b_l Y_{lm}^*(\hat{n}_2) Y_{lm}(\hat{n}_1) \quad (\text{B30})$$

$$(\text{B31})$$

we obtain a well known result:

$$b(\hat{n}_2, \hat{n}_1) = \sum_{l=0}^{\infty} \frac{(2l+1)}{4\pi} b_l P_l(\hat{n}_2 \cdot \hat{n}_1) \quad (\text{B32})$$

B.0.2. Gaussian model

Unity normalized gaussian beam.

$$B(\theta) = \exp\left(-\frac{1}{2} \frac{\theta^2}{\sigma^2}\right) \quad (\text{B33})$$

Solid angle normalized gaussian beam.

$$b(\theta) = \frac{1}{\Omega_B} \exp\left(-\frac{1}{2} \frac{\theta^2}{\sigma^2}\right) \quad (\text{B34})$$

This solid angle normalized beam can be expanded in terms of spherical harmonics,

$$b(\theta) = \sum_{l=0}^{l_{\max}} \sum_m \sqrt{\frac{(2l+1)}{4\pi}} b_{lm} Y_{lm}(\theta, \phi), \quad (\text{B35})$$

with the expansion coefficient given by the projection:

$$b_{lm} = \sqrt{\frac{4\pi}{(2l+1)}} \int d\Omega b(\theta, \phi) Y_{lm}^*(\theta, \phi) \quad (\text{B36})$$

due to $b(\theta)$ does not depend on ϕ coordinate (symmetric beam in the pointing direction), the unique modes with non vanishing contribution are the modes labeled with $m = 0$, then the coefficients $b_{lm} = b_l \delta_{0m}$:

$$b(\theta) = \sum_{l=0}^{l_{\max}} b_l Y_{l0}(\theta, \phi) \quad (\text{B37})$$

where b_l is approximately,

$$b_l = \exp\left(-\frac{\sigma^2 l^2}{2}\right) \quad (\text{B38})$$

and

$$\sigma = \frac{\pi}{180} \frac{\theta_{FWHM}}{\sqrt{8 \ln 2}} \text{ (in degrees).}$$

Expanding in terms on Legendre polynomials,

$$b(\theta) = \sum_{l=0}^{l_{\max}} b_l N_{l0} P_l(\cos \theta) \quad (\text{B39})$$

where N_{l0} are the normalization coefficients for spherical harmonics $N_{l0} = \sqrt{\frac{(2l+1)}{4\pi}}$ and $P_l(\cos \theta) = P_l^0(\cos \theta)$.

$$b(\hat{n} \cdot \hat{n}') = \sum_{l=0}^{l_{\max}} \frac{(2l+1)}{4\pi} b_l P_l(\hat{n} \cdot \hat{n}') \quad (\text{B40})$$

C. WINDOW FUNCTION FOR POLARIZATION

:

$$Q_b \pm iU_b = -b(\theta)e^{\pm 2i\phi} \quad (\text{C41})$$

this can be expanded:

$$\frac{1}{\sqrt{2}}(Q_b \pm iU_b) = \sum_{lm} \sqrt{\frac{2l+1}{4\pi}} (b_{lm}^G \mp ib_{lm}^C) \mp 2Y_{lm}(\theta, \phi) \quad (\text{C42})$$

$b_{lm}^E = -\sqrt{2}b_{lm}^G$ and $b_{lm}^B = -\sqrt{2}b_{lm}^C$

the beam response function for polarization is defined by

$${}_2b_l^p = 2b_{lm}^E \quad (\text{C43})$$

$$b_{l2}^G = \sqrt{\frac{4\pi}{(2l+1)}} \frac{M_{l2}}{2\sqrt{2}} \int d\Omega b(\theta) {}_{-2}P_l^2(\cos \theta) \quad (\text{C44})$$

$$b_{l2}^G = \frac{2\pi}{\sqrt{2}} \frac{(l-2)!}{(l+2)!} \int d\theta \sin \theta b(\theta) {}_{-2}P_l^2(\cos \theta) \quad (\text{C45})$$

$${}_2b_l^p = -(4\pi) \frac{(l-2)!}{(l+2)!} \int d\theta \sin \theta b(\theta) {}_{-2}P_l^2(\cos \theta) \quad (\text{C46})$$

$$\frac{1}{\sqrt{2}}(\tilde{Q} \pm i\tilde{U}) = \sum_{lm} {}_2b_l^p (a_{lm}^G \mp ia_{lm}^C) \mp 2Y_{lm}(\theta, \phi) \quad (\text{C47})$$